19th International Conference on
Adaptive Structures and Technologies
October 6-9, 2008
Ascona, Switzerland

Piezoelectric Energy Harvesting from Macro-Fiber Composites with an Application to Morphing-Wing Aircrafts

Alper Erturk[1]*, Onur Bilgen[2], Matthieu Fontenille[3], Daniel J. Inman[2]
Center for Intelligent Material Systems and Structures
[1] Department of Engineering Science and Mechanics, Virginia Tech, Blacksburg VA 24061 USA
[2] Department of Mechanical Engineering, Virginia Tech, Blacksburg VA 24061 USA
[3] Université de Technologie de Compiègne, Compiègne, France
* Corresponding author: 310 Durham Hall, Virginia Tech, Blacksburg, VA 24061, USA
Phone: 1 (540) 231-2910, Fax: 1 (540) 231-2903, E-mail: erturk@vt.edu

ABSTRACT

The use of piezoelectric materials for low-power generation has been investigated by several researchers over the last decade. Typically, unimorph and bimorph cantilevers with conventionally poled monolithic piezoceramics have been implemented for this purpose. The experimental and modeling efforts in the literature are mostly limited to these monolithic configurations. However, there are several excitation conditions and operation environments where the monolithic piezoceramic configurations cannot be used due to their extremely brittle nature. The macro-fiber composite (MFC) piezoceramic configuration overcomes this issue owing to its flexible and robust nature. This paper investigates the MFC configuration for piezoelectric energy harvesting and presents a distributed-parameter electromechanical model. MFC unimorph configuration is modeled based on the Euler-Bernoulli beam theory and it is assumed to be excited by the translation of its base in the transverse direction with superimposed small rotation. A resistive load is considered in the electrical circuit for simplicity. After deriving the governing differential equations, closed-form solutions for the coupled vibration response and the voltage response are obtained for harmonic base excitations. Model predictions are first verified for an MFC unimorph with a brass substrate and then validations are given for MFC unimorphs with various substrate materials and thicknesses. For the same type of MFC with three different substrate materials (brass, aluminum and stainless steel), it is shown that the maximum peak power at resonance excitation is obtained for the aluminum substrate. Experimental results for different substrates are predicted successfully by using the coupled analytical model proposed here. Finally, results from the preliminary wind tunnel experiments are presented for piezoelectric energy harvesting from a flow-excited morphing airfoil with MFCs.

Keywords: Piezoelectricity, energy harvesting, macro-fiber composites, coupled modeling

1. INTRODUCTION

Vibration-based energy harvesting has received a great attention over the past decade. Research motivation in this field is due to the reduced power requirement of small electronic components and the ultimate goal is to power such small electronic devices by using the vibration energy available in their environment. The three basic vibration-to-electric energy conversion mechanisms are the electromagnetic [1,2], electrostatic [3,4] and piezoelectric [5,6] transductions. The literature of the last five years shows that piezoelectric transduction has received the most attention for vibration-to-electricity conversion and four review articles focusing on piezoelectric energy harvesting have been published in the last four years [7-10]. The relevant experimental research and possible applications of piezoelectric energy harvesting can be found in the aforementioned review articles.

Typically, a piezoelectric energy harvester is a cantilevered beam with one or two monolithic piezoceramic layers (a unimorph or a bimorph). The harvester beam is located on a vibrating host structure and the dynamic strain induced in the piezoceramic layer(s) generates an alternating voltage output across the electrodes covering the piezoceramic layer(s). Several researchers have investigated modeling and applications of monolithic piezoceramics for piezoelectric energy harvesting. Although they are very commonly used in several applications, extremely brittle nature of conventional monolithic piezoceramics limits their applications only to certain excitation conditions and operation environment. Macro-fiber composites (MFCs) [11] developed at NASA Langley Research Center has provided a very *robust* and *flexible* alternative to the existing monolithic piezoceramics. MFCs have been used by several researchers for sensing, actuation and vibration control [12-14]. Recently, Sodano *et al* [15] compared the performance of an MFC sample for power generation against other configurations and observed the deficiency of the MFC in power generation due to its low capacitance. Even though this is the case, the MFC configuration has several advantages for use in energy harvesting applications. The interdigitated electrode configuration reduces the capacitance of MFCs, which is not favorable for piezoelectric energy harvesting. However, at the same time it allows using the favorable 33-mode of piezoelectricity. Furthermore, it is almost impossible to use monolithic ceramics under certain loading conditions. In particular, in development of multi-functional – load-bearing – piezoelectric energy harvesters, one cannot use monolithic piezoceramics due to their extremely brittle nature and the use of MFCs becomes inevitable.

The existing literature on analytical and numerical modeling of MFCs has focused on homogenization and characterization of their electrical and mechanical properties [14,16,17]. Most of the research in the literature has dealt with sensing and actuation applications of MFCs. This paper provides a detailed discussion and modeling effort for piezoelectric energy harvesting from MFCs. First, a distributed parameter electromechanical model is introduced for piezoelectric energy harvesting from MFC unimorphs. A recently introduced closed-form solution (for monolithic piezoceramic configurations) [18,19] is implemented here for modeling the coupled dynamics of the MFC configuration. The unimorph formulation given here can easily be extended to bimorph configurations as well. Modeling of MFC beams is more complicated than that of monolithic beams due to the non-uniform and piece-wise defined electric field. Certain assumptions have been made and correction factors have been introduced to implement the analytical solution to the MFC configuration. After obtaining the closed-form electrical and mechanical response expressions, an experimental verification is provided for an MFC unimorph with a brass substrate. Then, a set of MFC unimorphs with different substrate materials and thicknesses are tested and modeled. It is aimed to identify the best substrate material and thickness among a set of substrates for a fixed MFC type. Finally, results from the preliminary wind tunnel experiments are presented for piezoelectric energy harvesting from a flow-excited morphing airfoil with MFCs.

2. DERIVATION OF THE ELECTROMECHANICAL MODEL

2-1. Modeling assumptions

The origin of the coupled equations derived here is the distributed-parameter piezoelectric energy harvester model presented by Erturk and Inman [18,19]. The original formulation was given for a unimorph cantilever with a monolithic piezoceramic layer excited by the motion of its base [18]. Later the coupled model was extended to bimorph configurations and experimental validations were presented [19].

The modeling assumptions of the coupled distributed-parameter problem investigated here are as follows:

- Shear deformations and rotary inertia effects are negligible (i.e., Euler-Bernoulli beam assumptions). Typical piezoelectric unimorphs are thin beams with large length-to-thickness ratios and therefore this is a reasonable assumption.

- Mechanical behavior of the substrate and piezoceramic layers is linearly elastic and oscillations are geometrically small. Therefore, the substrate, epoxy and Kapton layers obey the Hooke's law,

$$T_s = Y_s S_s\,,\; T_e = Y_e S_e\,,\; T_k = Y_k S_k \tag{1}$$

where T is the bending stress component, S is the bending stress component and Y is the Young's modulus of the respective isotropic layer (substrate, epoxy or Kapton are denoted by subscripts *s*, *e* and *k* respectively).

The piezoceramic layer obeys the following linear constitutive relation which is reduced from the tensorial representation [20] based on the Euler-Bernoulli beam assumptions:

$$\begin{Bmatrix} T_3 \\ D_3 \end{Bmatrix} = \begin{bmatrix} \bar{c}_{33}^E & -\bar{e}_{33} \\ \bar{e}_{33} & \bar{\varepsilon}_{33}^S \end{bmatrix} \begin{Bmatrix} S_3 \\ E_3 \end{Bmatrix} \tag{2}$$

where T_3 is the stress component, D_3 is the electric displacement component, S_3 is the strain component, E_3 is the electric field component, $\bar{e}_{33}$ is the effective piezoelectric constant, $\bar{c}_{33}^E$ is effective elastic stiffness component (Young's modulus) at constant electric filed and $\bar{\varepsilon}_{33}^S$ is the effective permittivity component at constant strain. An over-bar denotes that the constant is the effective constant in plane-stress conditions and it is not the elasticity component. Here, the direction of the dominating mechanical strain and the direction of electric field are the same (3-direction) and it is the longitudinal (x) direction of the beam shown in Figure 1.

- Interdigitated electrodes are assumed to have negligible stiffness and mass contribution to the unimorph. Therefore the structure is mechanically uniform in the longitudinal direction.

- Epoxy layer boding the MFC and the substrate layers does not cause any shear between these two layers. This is a relatively critical assumption since the bonding epoxy layer can be as thick as the substrate layer in some cases.

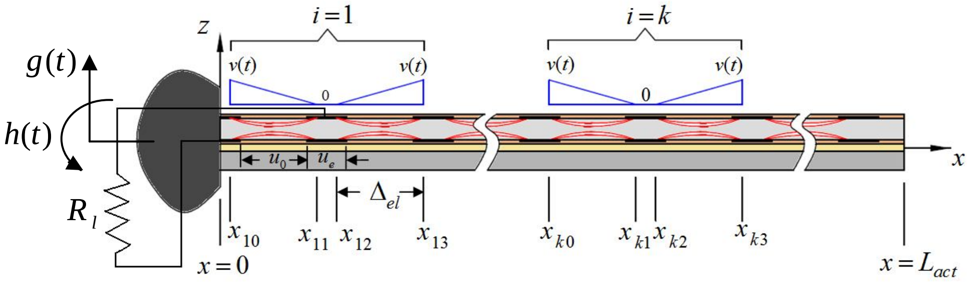

Figure 1. Unimorph MFC cantilever under base excitation (active length)

2-2. Governing equations of the coupled problem

2-2-1. Coupled mechanical equation

Free vibrations of the cantilevered MFC unimorph shown in Figure 1 are governed by the following partial differential equation:

$$\frac{\partial^2 M(x,t)}{\partial x^2} + c_s I \frac{\partial^5 w(x,t)}{\partial x^4 \partial t} + c_a \frac{\partial w(x,t)}{\partial t} + m \frac{\partial^2 w(x,t)}{\partial t^2} = 0 \tag{3}$$

where $M(x,t)$ is the internal bending moment (excluding the moment due to strain rate damping), $w(x,t)$ is the transverse deflection relative to the fixed frame, $c_s I$ is the strain-rate (internal) damping term, c_a is the viscous air (external) damping coefficient and *m* is the mass per unit length of the beam. Base excitation is given by

$$w_b(x,t) = g(t) + xh(t) \tag{4}$$

Here, $g(t)$ is the translation of the base in the transverse direction and $h(t)$ is the superimposed small rotation of the base. Transverse displacement response of the beam relative to the fixed frame can be expressed as

$$w(x,t) = w_b(x,t) + w_{rel}(x,t) \tag{5}$$

where $w_{rel}(x,t)$ is the transverse displacement response relative to the moving base and $w_b(x,t)$ is given by Equation (4). Substituting Equation (5) into Equation (3) gives a forced partial differential equation for the relative response, $w_{rel}(x,t)$:

$$\frac{\partial^2 M(x,t)}{\partial x^2} + c_s I \frac{\partial^5 w_{rel}(x,t)}{\partial x^4 \partial t} + c_a \frac{\partial w_{rel}(x,t)}{\partial t} + m \frac{\partial^2 w_{rel}(x,t)}{\partial t^2} = -m \frac{\partial^2 w_b(x,t)}{\partial t^2} - c_a \frac{\partial w_b(x,t)}{\partial t} \tag{6}$$

After expressing the strain component in terms of the curvature and the electric field in terms of the voltage ($E_3(t) = -v(t)/\Delta_{el}$ where $v(t)$ is the voltage across the interdigitated electrodes and Δ_{el} is the effective electrode spacing in Figure 1) one can integrate the moment of axial stress over the cross-section of the beam and this process yields one term related to the bending stiffness of the beam and one term related to piezoelectric coupling:

$$YI \frac{\partial^4 w(x,t)}{\partial x^4} + c_s I \frac{\partial^5 w(x,t)}{\partial x^4 \partial t} + c_a \frac{\partial w(x,t)}{\partial t} + m \frac{\partial^2 w(x,t)}{\partial t^2} + v(t) \frac{d^2 \Gamma(x)}{dx^2} = -m \frac{\partial^2 w_b(x,t)}{\partial t^2} - c_a \frac{\partial w_b(x,t)}{\partial t} \tag{7}$$

where the expression for the bending stiffness (*YI*) is obtained from cross-section transformation (homogenization) and $\Gamma(x)$ accounts for the spatial distribution of the electric potential:

$$\Gamma(x) = \vartheta \sum_{i=1}^{N_e} \left\{ \left(1 + \frac{x - x_{i0}}{x_{i0} - x_{i1}} \right) \left[H\left(x - x_{i0}\right) - H\left(x - x_{i1}\right) \right] + \left(\frac{x - x_{i2}}{x_{i3} - x_{i2}} \right) \left[H\left(x - x_{i2}\right) - H\left(x - x_{i3}\right) \right] \right\} \tag{8}$$

Here, N_e is the number of electrode pairs over the beam length ($N_e \cong L_{act} / 2\left(u_e + u_0\right)$ where L_{act} is the active beam length, u_e is the width of each electrode in the direction of beam axis, u_0 is the width of each non-electroded region in the direction of beam axis), $H(x)$ is the Heaviside function and ϑ is a coupling constant. According to Equation (8), at an arbitrary instant of the motion, the electric potential is assumed to be linearly decreasing from $v(t)$ to 0 in $x_{i0} \le x \le x_{i1}$ whereas it is assumed to be linearly increasing from 0 to $v(t)$ in $x_{i2} \le x \le x_{i3}$. The coupling treatment given by Equation (8) is a summation of N_e terms due to the piezoelectric coupling on small fiber elements. Therefore, the positions x_{i0}, x_{i1}, x_{i2} and x_{i3} change with the index *i*. As one moves from the clamped end to the free end, the index number increases as shown in Figure 1. For instance, starting from the clamped end,

For $i=1$; $x_{10} = \frac{u_e}{4}$, $x_{11} = x_{10} + u_0 + \frac{u_e}{2}$, $x_{12} = x_{11} + \frac{u_e}{2}$, $x_{13} = x_{12} + u_0 + \frac{u_e}{2}$;

For $i=2$; $x_{20} = x_{13} + \frac{u_e}{2}$, $x_{21} = x_{20} + u_0 + \frac{u_e}{2}$, $x_{22} = x_{21} + \frac{u_e}{2}$, $x_{23} = x_{22} + u_0 + \frac{u_e}{2}$;

For $i=k$; $x_{k0} = x_{(k-1)3} + \frac{u_e}{2}$, $x_{k1} = x_{k0} + u_0 + \frac{u_e}{2}$, $x_{k2} = x_{k1} + \frac{u_e}{2}$, $x_{k3} = x_{k2} + u_0 + \frac{u_e}{2}$; (9)

and so on for $i = 1 \ldots N_e$ with the increasing index number until the end of the active length (Figure 1).

The coupling constant in Equation (8) is given by

$$\vartheta = -\frac{\bar{e}_{33} b_{pt} \left[\left(h_d - \alpha h_p \right)^2 - \left(h_c + \alpha h_p \right)^2 \right]}{2\Delta_{el}} \tag{10}$$

where b_{pt} is the total width of the piezoceramic fibers, h_p is the thickness of the piezoceramic fibers, h_c is the position of the bottom of the piezoceramic layer from the neutral axis, h_d is the position of the top of the piezoceramic layer from the neutral axis and the effective electrode spacing is given by $\Delta_{el} = u_0 + u_e / 2$. Note that, the electric field is assumed to be uniform over the effective electrode spacing Δ_{el}. The form of the coupling constant given by Equation (10) is similar to the coupling constant given for a unimorph cantilever with a monolithic ceramic layer [18] where the electric field is uniform and the 31-mode is used instead of the 33-mode with non-uniform electric field. In Equation (10), α is an empirical correction factor that reduces the thickness of the piezoceramic to an effective value due to the non-uniform distribution of the electric field over the thickness. In other words, α reduces the physical piezoceramic thickness that causes the piezoelectrically induced bending moment with non-uniform electric field to a cross-section with a uniform electric field distribution having the equivalent bending moment (it can take values between 0 and 0.5). As discussed in Section 3, an average value of $\alpha \cong 0.2$ is identified by matching the model predictions for a set of experiments using M 8507 P1 type MFC [21] with different substrates (which corresponds to a 40 % thickness reduction). Clearly, this approximation is defined for a specified effective electrode spacing ($\Delta_{el} = u_0 + u_e / 2$). If one defines the effective electrode spacing differently (e.g., $\Delta_{el} = u_0 + u_e$), a different value would be identified for α. The former expression is preferred here for the effective electrode spacing (Figure 1).

2-2-2. Coupled electrical equation

As can be seen from Figure 1, the electrical circuit consists of a resistive electrical load (R_l) only (in addition to the inherent capacitance of the MFC piezoceramic). Therefore the circuit that the MFC piezoceramic operates into has an admittance of $1/R_l$. From the IEEE standard on piezoelectricity [20], one can write

$$\frac{d}{dt}\left(\int_A \mathbf{D}\cdot\mathbf{n}dA\right)=\frac{v(t)}{R_l} \tag{11}$$

where $v(t)$ is the voltage across the resistive load, $\mathbf{D}$ is the vector of electric displacements, $\mathbf{n}$ is the unit outward normal on the electrode surface and the integration is performed over the electrode area (Figure 2). It should be noted from Figures 1 and 2 that the middle electrode finger in each electrode pair is assumed to have zero electric potential as a convention. This way the resulting potential difference (voltage) across the resistive load is directly $v(t)$. One could as well assume two different potentials as $v_1(t)$ and $v_2(t)$ such that the variation in between is still linear and the voltage across the resistive load is the difference between these potentials. However, we use the former approach in the formulation given here.

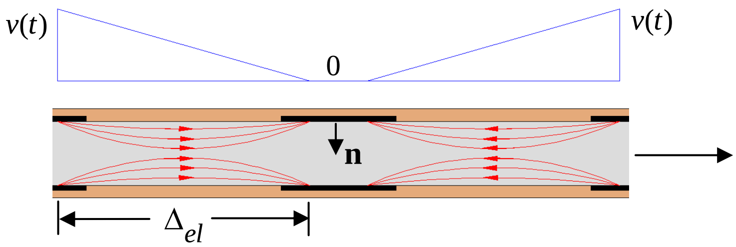

Figure 2. Enlarged view of a section showing the non-uniform electric field lines and the assumed (linear) electric potential distribution

In the constitutive relation given by Equation (2), D_3 was assumed to be the only nontrivial component of electric displacement vector. It should be noted from Figure 2 that the electric field lines are almost in the 3-direction (x-direction) away from the electrodes whereas they make an angle with the electrode surface in the vicinity of the electrodes. Therefore, we introduce a correction factor (β) to account for the angle between the electric displacement component and the surface normal on the electrode surface. After substituting the second row of Equation (2) into Equation (11), the latter equation becomes:

$$C_p\frac{dv(t)}{dt}+\frac{v(t)}{R_l}=-\left(h_{pc}+\frac{h_p}{4}\right)\int_A \bar{e}_{33}\frac{\partial^3 w_{rel}(x,t)}{\partial x^2\partial t}\beta dA-\left(h_{pc}-\frac{h_p}{4}\right)\int_A \bar{e}_{33}\frac{\partial^3 w_{rel}(x,t)}{\partial x^2\partial t}\beta dA \tag{12}$$

where C_p is the capacitance of the MFC (overhang region), h_{pc} is the center of the piezoceramic from the neutral axis and the two integrals on the right-hand side of Equation (12) are for the lower and the upper electrode pairs. Because the electric displacement component is not perpendicular to the electrode surface, the correction factor β has the effect of reducing the charge collocated by the electrodes (using $\beta \cong 0.5$ for M 8507 P1 type MFC results in accurate model predictions for different substrate materials as shown in Sections 3 and 4).

Equation (12) can be rewritten as

$$C_p \frac{dv(t)}{dt} + \frac{v(t)}{R_l} = -2\beta \bar{e}_{33} h_{pc} \int_A \frac{\partial^3 w_{rel}(x,t)}{\partial x^2 \partial t} dA \tag{13}$$

The integral expression in Equation (13) can be expanded according to the region covered by the electrodes in Figure 1:

$$C_p \frac{dv(t)}{dt} + \frac{v(t)}{R_l} = -2\beta \bar{e}_{33} h_{pc} b_{pt} \left(\int_{x_{i0}-u_e/4}^{x_{i0}+u_e/4} \frac{\partial^3 w_{rel}(x,t)}{\partial x^2 \partial t} dx + \int_{x_{i1}-u_e/4}^{x_{i2}+u_e/4} \frac{\partial^3 w_{rel}(x,t)}{\partial x^2 \partial t} dx + \int_{x_{i3}-u_e/4}^{x_{i3}+u_e/4} \frac{\partial^3 w_{rel}(x,t)}{\partial x^2 \partial t} dx \right) \tag{14}$$

2-2-3. Modal analysis

The vibration response of the MFC unimorph relative to its base can be represented as an absolutely and uniformly convergent series of the eigenfunctions as

$$w_{rel}(x,t) = \sum_{r=1}^{\infty} \phi_r(x) \eta_r(t) \tag{15}$$

where $\phi_r(x)$ and $\eta_r(t)$ are the mass normalized eigenfunction and the modal mechanical response of the clamped-free beam for the *r*th mode, respectively. Based on the proportional damping assumption (strain-rate damping is assumed to be stiffness-proportional whereas air damping is assumed to be mass-proportional), the eigenfunctions of the proportionally damped system become the eigenfunctions of the respective undamped system:

$$\phi_r(x) = \sqrt{\frac{1}{mL}} \left[\cosh \frac{\lambda_r}{L} x - \cos \frac{\lambda_r}{L} x - \sigma_r \left(\sinh \frac{\lambda_r}{L} x - \sin \frac{\lambda_r}{L} x \right) \right] \tag{16}$$

where the dimensionless frequency numbers (λ_r) are obtained from

$$1 + \cos\lambda \cosh\lambda = 0 \tag{17}$$

and σ_r is expressed as

$$\sigma_r = \frac{\sinh\lambda_r - \sin\lambda_r}{\cosh\lambda_r + \cos\lambda_r} \tag{18}$$

Moreover, ω_r is the undamped natural frequency of the *r*th mode:

$$\omega_r = \lambda_r^2 \sqrt{\frac{YI}{mL^4}} \tag{19}$$

which is approximately the resonance frequency of the unimorph (for light mechanical damping) when the MFC is in short circuit conditions. Note that the mass-normalized eigenfunctions satisfy the following orthogonality conditions:

$$\int_{x=0}^{L} m\phi_s(x)\phi_r(x)dx = \delta_{rs}\,, \quad \int_{x=0}^{L} YI\phi_s(x)\frac{d^4\phi_r(x)}{dx^4}dx = \omega_r{}^2\delta_{rs} \tag{20}$$

2-2-4. Governing equations in modal coordinates

Equations (7) and (14) are the electromechanically coupled equations of the unimorph cantilever under base excitation. Substituting Equation (15) into Equation (7) and employing the orthogonality conditions of the eigenfunctions yield

$$\frac{d^2\eta_r(t)}{dt^2} + 2\zeta_r\omega_r\frac{d\eta_r(t)}{dt} + \omega_r{}^2\eta_r(t) + \chi_r v(t) = N_r(t) \tag{21}$$

where

$$\chi_r = \int_0^L \phi_r(x)\frac{d^2\Gamma(x)}{dx^2}dx = \vartheta\sum_{i=1}^{N_e}\left(\frac{\phi_r(x_{i0}) - \phi_r(x_{i1})}{x_{i0} - x_{i1}} + \frac{\phi_r(x_{i2}) - \phi_r(x_{i3})}{x_{i3} - x_{i2}} + \left.\frac{d\phi_r(x)}{dx}\right|_{x_{i0}}^{x_{i3}}\right) \tag{22}$$

is the modal coupling term and

$$\zeta_r = \frac{c_s I\omega_r}{2YI} + \frac{c_a}{2m\omega_r} \tag{23}$$

is the modal mechanical damping ratio that includes the effects of both strain rate damping and viscous air damping. It is clear from Equation (23) that strain-rate damping is assumed to be proportional to the bending stiffness of the beam whereas air damping is assumed to be proportional to the mass per unit length of the beam.

The modal mechanical forcing function in Equation (21) can be expressed as

$$N_r(t) = N_r^m(t) + N_r^c(t) \tag{24}$$

Here, the components of mechanical excitation (which are the inertial and the damping excitation terms) are given by the following expressions, respectively,

$$N_r^m(t) = -m\left(\gamma_r^w\frac{d^2g(t)}{dt^2} + \gamma_r^\theta\frac{d^2h(t)}{dt^2}\right),\ N_r^c(t) = -c_a\left(\gamma_r^w\frac{dg(t)}{dt} + \gamma_r^\theta\frac{dh(t)}{dt}\right) \tag{25}$$

where

$$\gamma_r^w = \int_{x=0}^{L}\phi_r(x)dx\,,\ \gamma_r^\theta = \int_{x=0}^{L}x\phi_r(x)dx \tag{26}$$

Typically, for harvesters operating in air, excitation due to the external damping is negligible when compared to the inertial excitation (i.e., $N_r^c(t) \ll N_r^m(t)$) and one can simply set $N_r^c(t) = 0$.

Equation (15) can be substituted into Equation (14) to give

$$C_p \frac{dv(t)}{dt} + \frac{v(t)}{R_l} = \sum_{r=1}^{\infty} \kappa_r \frac{d\eta_r(t)}{dt} \tag{27}$$

where

$$\kappa_r = -2\beta\overline{e}_{33} h_{pc} b_{pt} \sum_{i=1}^{N_e} \left(\left. \frac{d\phi_r(x)}{dx} \right|_{x_{i0}-u_e/4}^{x_{i0}+u_e/4} + \left. \frac{d\phi_r(x)}{dx} \right|_{x1-u_e/4}^{x_{i2}+u_e/4} + \left. \frac{d\phi_r(x)}{dx} \right|_{x_{i3}-u_e/4}^{x_{i3}+u_e/4} \right) \tag{28}$$

Equations (21) and (27) are the piezoelectrically coupled equations of the unimorph in modal coordinates.

2-3. Steady-state electromechanical response to harmonic excitation

If the base motion is harmonic of the form $g(t) = Y_0 e^{j\omega t}$ and $h(t) = \theta_0 e^{j\omega t}$ such that $w_b(x,t) = \left(Y_0 + x\theta_0\right) e^{j\omega t}$ (where Y_0 and θ_0 are the amplitudes of the base translation and rotation, respectively, ω is the driving frequency and j is the unit imaginary number), modal mechanical response and the voltage response take the following forms at steady state:

$$\eta_r(t) = \mathrm{H}_r e^{j\omega t}, \; v(t) = V_0 e^{j\omega t} \tag{29}$$

where H_r is the complex modal mechanical response amplitude and V_0 is the complex voltage response amplitude. Using these relations in Equation (21) gives

$$\left(\omega_r^{\,2} - \omega^2 + 2\zeta_r \omega_r\right) \mathrm{H}_r + \chi_r V_0 = F_r \tag{30}$$

where

$$F_r = m\omega^2 \left(\gamma_r^w Y_0 + \gamma_r^\theta \theta_0\right) - jc_a\omega\left(\gamma_r^w Y_0 + \gamma_r^\theta \theta_0\right) \tag{31}$$

Similarly, from Equation (27), one obtains

$$\left(\frac{1}{R_l} + j\omega C_p\right) V_0 = j\omega \sum_{r=1}^{\infty} \kappa_r \mathrm{H}_r \tag{32}$$

One can extract H_r in Equation (30) and substitute that into Equation (30) to obtain the complex voltage amplitude V_0, yielding

$$v(t) = \frac{\displaystyle\sum_{r=1}^{\infty} \frac{j\omega\kappa_r F_r}{\omega_r^{\,2} - \omega^2 + j2\zeta_r \omega_r \omega}}{\displaystyle\frac{1}{R_l} + j\omega C_p + \sum_{r=1}^{\infty} \frac{j\omega\kappa_r \chi_r}{\omega_r^{\,2} - \omega^2 + j2\zeta_r \omega_r \omega}} e^{j\omega t} \tag{33}$$

Then, H_r is obtained by substituting V_0 into Equation (31), which eventually gives the following relation from Equation (15):

$$w_{rel}(x,t)=\sum_{r=1}^{\infty}\left[\left(F_r-\chi_r\frac{\displaystyle\sum_{r=1}^{\infty}\frac{j\omega\kappa_r F_r}{\omega_r^{\ 2}-\omega^2+j2\zeta_r\omega_r\omega}}{\displaystyle\frac{1}{R_l}+j\omega C_p+\sum_{r=1}^{\infty}\frac{j\omega\kappa_r\chi_r}{\omega_r^{\ 2}-\omega^2+j2\zeta_r\omega_r\omega}}\right)\frac{\phi_r(x)e^{j\omega t}}{\omega_r^{\ 2}-\omega^2+j2\zeta_r\omega_r\omega}\right] \tag{34}$$

Equation (34) is the vibration response of the unimorph relative to its moving base. Equation (34) can be used in Equation (5) to obtain the vibration response relative to the fixed frame.

3. MODEL VERIFICATION

3-1. Analytical FRFs

If the base of the unimorph does not rotate (i.e., $h(t)=\theta_0 e^{j\omega t}=0$) and the component of excitation due to external damping is negligible, Equation (31) reduces to

$$F_r=\gamma_r^w m\omega^2 Y_0 \tag{35}$$

Then, the voltage output – to – base acceleration FRF can be extracted from Equation (33) as

$$\mu(\omega)=\frac{v(t)}{-\omega^2 Y_0 e^{j\omega t}}=\frac{\displaystyle\sum_{r=1}^{\infty}\frac{-j\omega m\kappa_r\gamma_r^w}{\omega_r^{\ 2}-\omega^2+j2\zeta_r\omega_r\omega}}{\displaystyle\frac{1}{R_l}+j\omega C_p+\sum_{r=1}^{\infty}\frac{j\omega\kappa_r\chi_r}{\omega_r^{\ 2}-\omega^2+j2\zeta_r\omega_r\omega}} \tag{36}$$

Similarly, the relative displacement – to – base acceleration FRF is extracted from Equation (34):

$$\psi(\omega,x)=\frac{w_{rel}(x,t)}{-\omega^2 Y_0 e^{j\omega t}}=\sum_{r=1}^{\infty}\left[\left(\gamma_r^w-\chi_r\frac{\displaystyle\sum_{r=1}^{\infty}\frac{j\omega\kappa_r\gamma_r^w}{\omega_r^{\ 2}-\omega^2+j2\zeta_r\omega_r\omega}}{\displaystyle\frac{1}{R_l}+j\omega C_p+\sum_{r=1}^{\infty}\frac{j\omega\kappa_r\chi_r}{\omega_r^{\ 2}-\omega^2+j2\zeta_r\omega_r\omega}}\right)\frac{-m\phi_r(x)}{\omega_r^{\ 2}-\omega^2+j2\zeta_r\omega_r\omega}\right] \tag{37}$$

It is worthwhile to mention that the laser vibrometer measures the absolute velocity of the beam at the measurement point $x=L_m$. Therefore, the FRF given by Equation (37) must be modified as follows to give the absolute velocity response per base acceleration:

$$\psi_{\text{modified}}(\omega,L_m)=\frac{\dfrac{dw(L_m,t)}{dt}}{-\omega^2 Y_0 e^{j\omega t}}=\frac{\dfrac{d}{dt}\left[Y_0 e^{j\omega t}+w_{rel}(L_m,t)\right]}{-\omega^2 Y_0 e^{j\omega t}}=\frac{1}{j\omega}+j\omega\psi(\omega,L_m) \tag{38}$$

which is evaluated at the measurement point of the laser vibrometer.

3-2. Experimental setup

The experimental setup used for model verifications is shown in Figure 3a. The MFC unimorph is excited from its base by means of an LDS electromagnetic shaker. The base acceleration of the harvester is measured by a low mass accelerometer (PCB U352C22) and the velocity response of the harvester at the free end is measured by a laser vibrometer (Polytec OFV303 laser head, OFV3001 vibrometer). 13 different resistive loads have been used in the experiments: 1.2, 4.7, 9.9, 21.5, 37.5, 44.9, 90.9, 179.5, 247.8, 319.2, 429.3, 685.1 and 995 kohms. Note that the input resistance of the data acquisition system (SigLab) is measured as 995 kohms. Therefore, this value cannot be exceeded in the experiments with this data acquisition unit. Coherence plots for the velocity and voltage FRFs for all resistive loads are plotted in Figure 3b and the coherence is very good except for very low frequencies (less than 20 Hz).

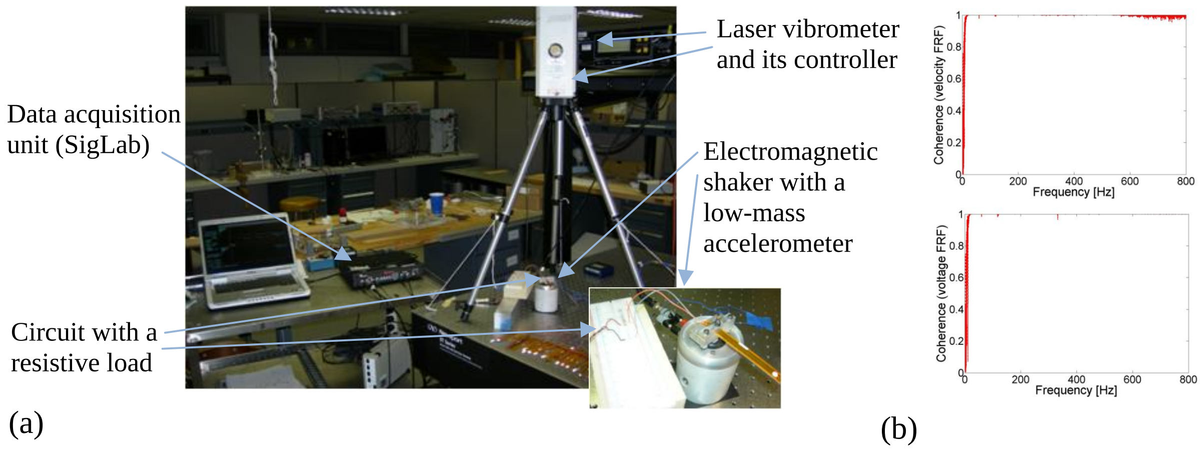

Figure 3. (a) Experimental setup used for testing of an MFC unimorph and the (b) coherence plots of the velocity and voltage measurements

The MFC unimorph investigated in this section has a brass substrate of 0.0762 mm thickness and the MFC layer is M 8507 P1 manufactured by the Smart Material Corporation [21]. This piezoceramic uses Navy Type II type (PZT-5A) piezoceramics. For the typical data of PZT-5A from the literature, plane-stress value of the piezoelectric constant is $\bar{e}_{33} = 19.1\,\mathrm{C/m^2}$ and that of the elastic stiffness at constant electric field is $\bar{c}_{33}^{E} = 64\,\mathrm{GPa}$. The reported value [21] of capacitance is 2.27 nF for the entire active region (for the free active length of 85 mm). Since the clamped region of the MFC is inactive, the effective capacitance is 1.95 nF from 2.27(73/85) nF where 73 mm is the active overhang length in the clamped condition). The epoxy type used for bonding the substrate and MFC layers is 3M DP460 and its shear strength is 4500 psi (~31 MPa). The geometric parameters of the MFC unimorph are listed in Table 1. The substrate material (brass) is assumed to have a Young's modulus of 105 GPa and a mass density of 9000 kg/m^3. For the epoxy and Kapton materials, a Young's modulus of 3 GPa is assumed (which is much less than the Young's moduli of the piezoceramic and substrate) in the bending stiffness (YI) calculations. Total mass per length of the MFC and the bonding epoxy layer are extracted experimentally as 0.0123 kg/m. The laser vibrometer measures the velocity response at $L_m = 74\,\mathrm{mm}$. For this MFC sample, the correction factors of the analytical model described in Section 2 are identified as $\alpha \cong 0.2$ and $\beta \cong 0.5$, and validity of these factors is observed for different substrate materials.

Table 1. Geometric parameters of the MFC unimorph with a brass substrate

Total overhang length, L [mm]	80.5
Overhang length of the active region, L_{act} [mm]	73
Width of the substrate, b_s [mm]	16
Width of the active region, b_{act} [mm]	7.3
Thickness of each piezoceramic fiber, h_p [mm]	0.18
Width of each piezoceramic fiber, b_p [mm]	0.355
Width of each epoxy fiber, b_{ep} [mm]	0.0513
Number of piezoceramic fibers, N_p	18
Electrode width in the length direction, u_e [mm]	0.097
Electrode spacing in the length direction, u_0 [mm]	0.41
Effective electrode spacing, Δ_{el} [mm]	0.046
Number of electrode pairs, N_e	72
Thickness of each Kapton layer (in the active region) , h_{ka} [mm]	0.06
Thickness of the Kapton in the inactive region, h_{ki} [mm]	0.12
Thickness of the substrate, h_s [mm]	0.0762
Thickness of the epoxy layer, h_{ep} [mm]	0.028

3-3. Model predictions and experimental results

For the set of electrical loads used, the experimental voltage – to – base acceleration and tip velocity – to – base acceleration FRFs are plotted along with the analytical predictions in Figure 4. The analytical FRFs in Figure 4a are generated using Equation (36) whereas those in Figure 4b are generated using Equation (38). Modal mechanical damping ratios are identified for a fixed resistive load as $\zeta_1 = 0.0085$, $\zeta_2 = 0.0075$, and $\zeta_3 = 0.011$ for the first three vibration modes. The first three natural frequencies of the unimorph (28.4 Hz, 178.8 Hz, and 489.7 Hz in short circuit conditions) are predicted with relative errors of 0.4 %, 0.06 % and 2.3 % for modes 1, 2, and 3, respectively.

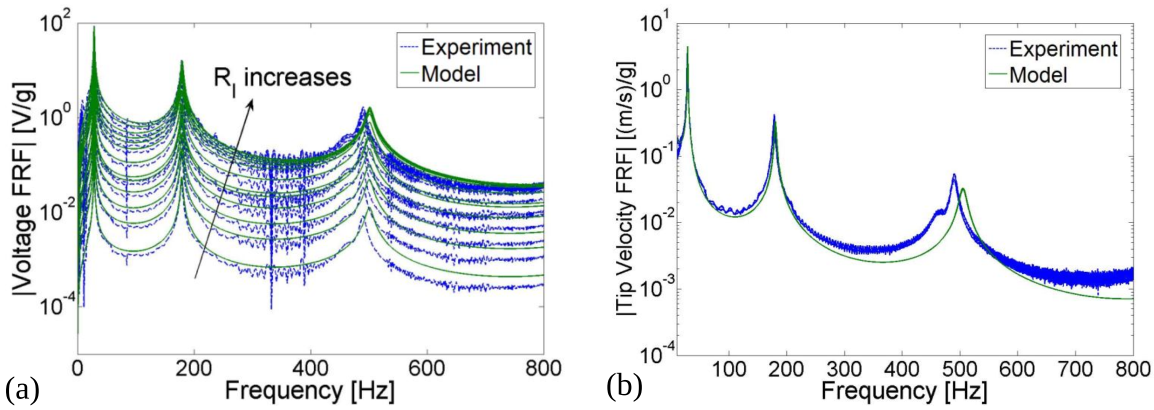

Figure 4. (a) Voltage FRFs and (b) tip velocity FRFs for 13 different resistive loads

Figure 5 shows detailed views of the voltage FRF around the first three modal frequencies of the MFC unimorph. Note that the model predictions are in very good agreement with the experimental results especially in the first two modes. It should be noted that, for the geometric parameters given in Table 1, the length-to-thickness aspect ratio of the MFC unimorph is about 200. Therefore, for these practical modes, structral shear deformations are not expected to be pronounced. The inaccuracy in the model predictions around the third vibration mode is attributed to the shear effects in the bonding epoxy layer.

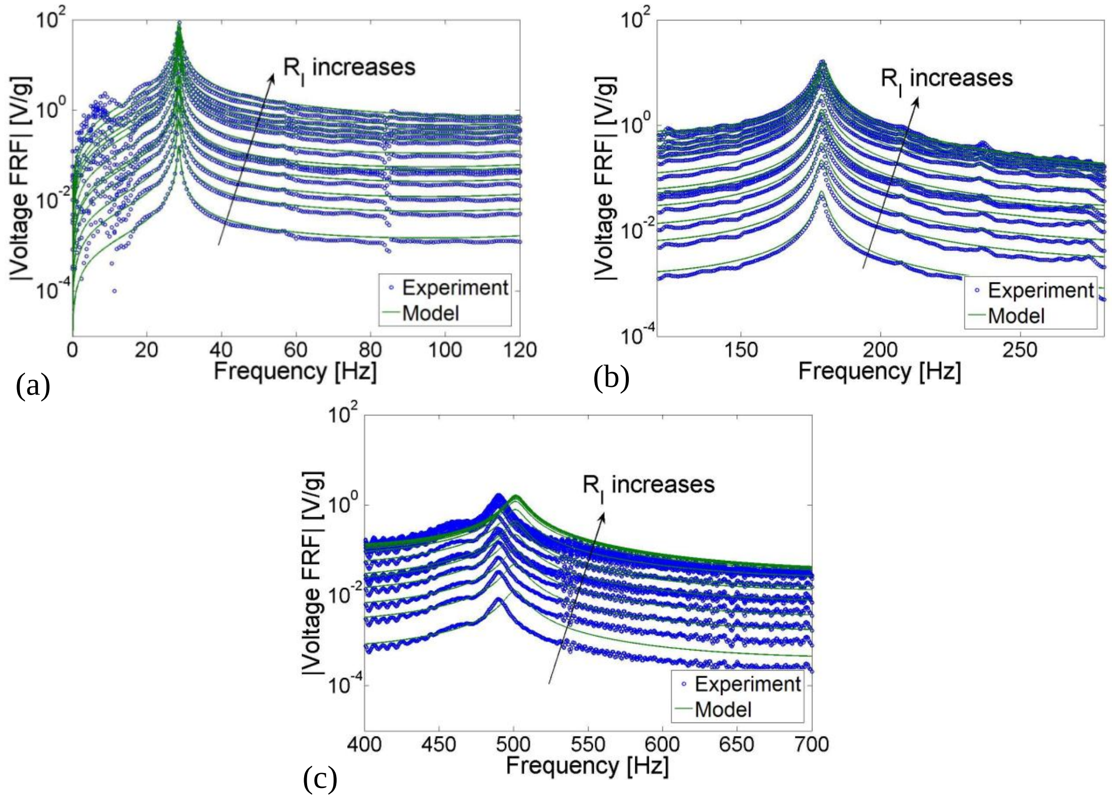

Figure 5. Detailed views from the voltage FRF around different vibration modes; (a) mode 1, (b) mode 2 and (c) mode 3

Variation of the peak electrical voltage out with load resistance for excitation at the short circuit resonance frequency of the first vibration mode (28.4 Hz) is plotted in Figure 6a. The voltage output of the MFC unimorph increases from 0.13 Volts/*g* to 87 Volts/*g* as load resistance is increased from 1.2 kohms to 995 kohms. This graphs is then used to plot the variation of the peak power with load resistance as shown in Figure 6b. The maximum power is obtained as 7.6 mW/g^2 for the largest resistive load used (995 kohms). As mentioned before, the maximum resistive load used in the experiments is restricted by the input resistance of the data acquisition system (which is 995 kohms). It is clear from Figure 6b that the optimum load resistance of this unimorph is greater than this value. Yet this data acquisition system does not allow esimating the optimum load resistance experimentally. It can analytically be shown that the optimum load resistance of this sample for excitation at 28.4 Hz is approximately 2.35 Mohms.

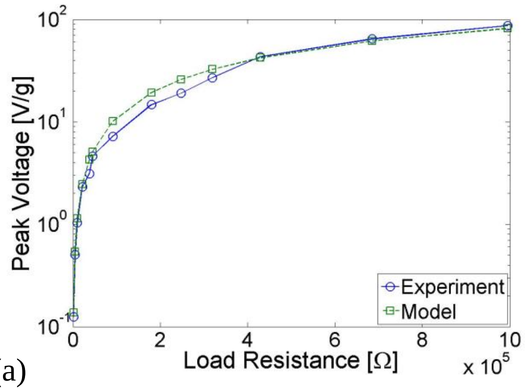

(a)

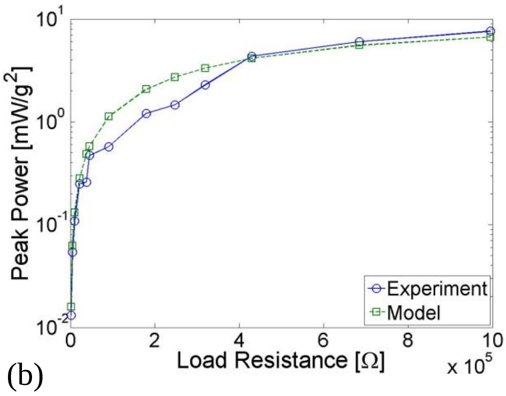

(b)

Figure 6. Variations of the (a) peak voltage and (b) peak power with electrical load resistance for excitation at the short circuit resonance frequency of the first mode (28.4 Hz)

4. THE EFFECT OF SUBSTRATE MATERIAL AND THICKNESS ON PIEZOELECTRIC POWER GENERATION

4-1. Experimental setup

A set of MFC unimorphs with different substrate materials and thicknesses is tested and modeled in this section to investigate the variation of the electrical power output with substrate material and thickness. The MFC type is the same as the one that was tested and modeled in the previous section (M 8507 P1). The experimental setup used for testing the samples under base excitation is shown in Figure 6a and it is very similar to the setup shown in Figure 3a (a laser vibrometer, electromagnetic shaker with a low-mass accelerometer for base excitation, a resistive electrical load in the circuit and the data acquisition system). The MFC unimorphs tested and modeled are shown in Figure 6b. These 9 samples use 3 different substrate materials (brass, aluminum and stainless steel) with 3 different thicknesses (0.002”, 0.003” and 0.004” or 50.8 μm, 76.2 μm and 101.6 μm). Overhang length of each unimorph is approximately 80 mm. Other than the substrate thickness and the thickness of the epoxy layer between the MFC and the substrate, the geometric parameters are as given in Table 1. Average epoxy thickness for each sample is shown in Table 2. Note that, typically, the epoxy thickness for each sample shows a large deviation over the length of the beam and it is an important source of inaccuracy in model predictions.

(a) 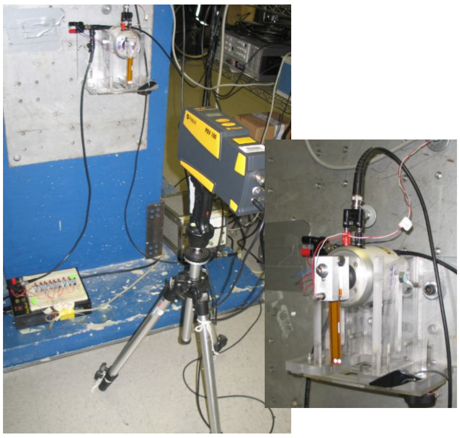

(b) 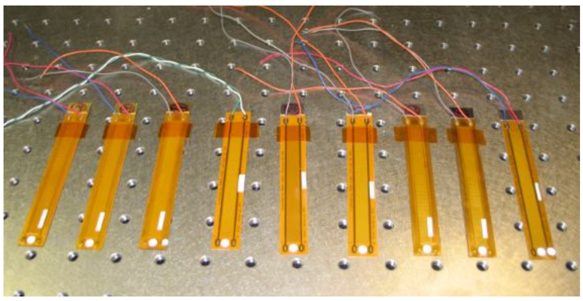

Figure 7. (a) Experimental setup used for testing the MFC unimorphs and the (b) MFC unimorphs with different substrates

In the following sections, the power outputs for different substrate thicknesses are compared with each other for different substrates. In all cases, the MFC is assumed to be excited at its first short circuit resonance frequency. Model predictions are plotted along with the experimental results. Finally, the power outputs of different substrates are compared with each other and the best substrate material and thickness are identified among the samples used here.

Table 2. Thickness of the epoxy layer for each unimorph

Substrate material	Substrate thickness [mm]	Average epoxy thickness [mm]
Brass	0.0508	0.010
Brass	0.0762	0.028
Brass	0.1016	0.033
Aluminum	0.0508	0.015
Aluminum	0.0762	0.018
Aluminum	0.1016	0.019
Steel	0.0508	0.020
Steel	0.0762	0.018
Steel	0.1016	0.059

4-2. Brass substrates

The fundamental resonance frequency of the MFC unimorphs with brass substrates changes from 25.4 Hz to 30.5 Hz as the substrate thickness is increased from 50.8 μm to 101.6 μm. As can be seen from Figure 8, the maximum voltage and power outputs for each resistive load are obtained for a 76.2 mm substrate thickness. Model predictions are in very good agreement with the experimental results.

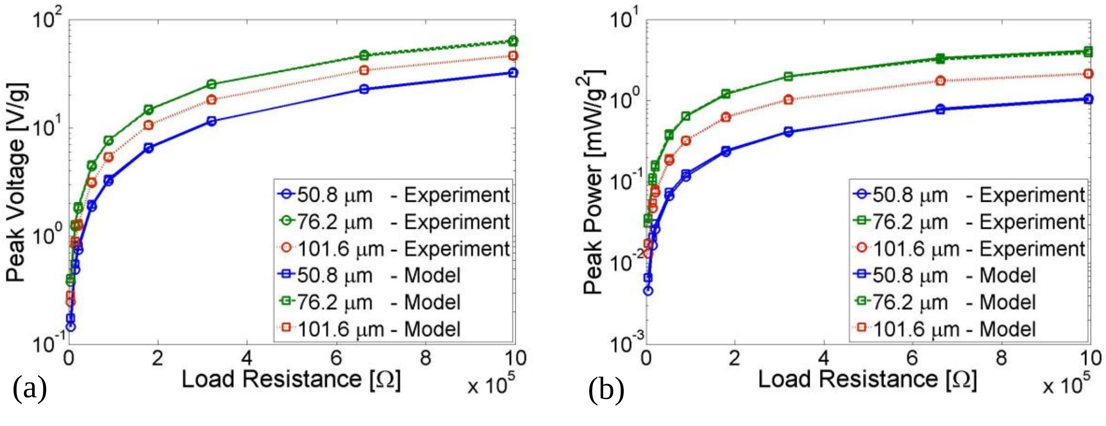

Figure 8. Variations of the (a) peak voltage and (b) peak power outputs of the MFCs with brass substrates with electrical load resistance for excitation at the short circuit resonance frequency of the first mode

4-3. Aluminum substrates

For the MFC unimorphs with aluminum substrates, the fundamental resonance frequency changes from 27.6 Hz to 34.2 Hz as the substrate thickness is increased from 50.8 μm to 101.6 μm. As in the previous case, Figure 9 shows that the maximum voltage and power outputs for each resistive load are obtained for a 76.2 mm substrate thickness. The model predictions are successful.

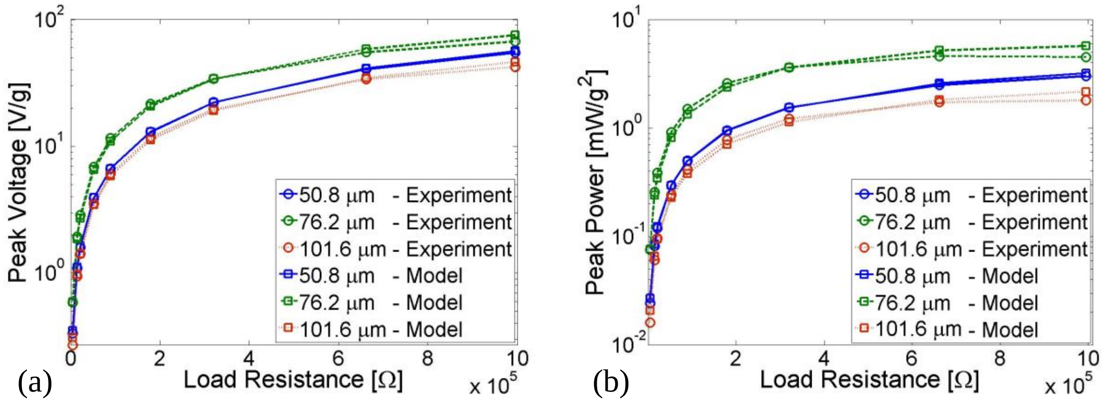

Figure 9. Variations of the (a) peak voltage and (b) peak power outputs of the MFCs with aluminum substrates with electrical load resistance for excitation at the short circuit resonance frequency of the first mode

4-4. Stainless steel substrates

As the substrate thickness is increased from 50.8 μm to 101.6 μm, the short circuit resonance frequency of the MFC unimorphs changes from 30.5 Hz to 38 Hz. The analytical model is again very successful in predicting the results for two of the substrate thicknesses (50.8 μm and 76.2 μm), however, it deviates from the experimental results of the case with a 101.6 μm thick substrate. The unexpected trend of this sample is more evident in Figure 10b for the peak power graph. When the epoxy thickness of this sample is checked from Table 2, it turns out to be much larger than the other samples. There might as well be other reasons (or defects) that make this sample behave in a way that cannot be predicted by the model especially for large resistive loads. Yet, in the experimental results of Figure 10b, the maximum power is still obtained for a 76.2 μm substrate thickness as in the cases of brass and aluminum substrates.

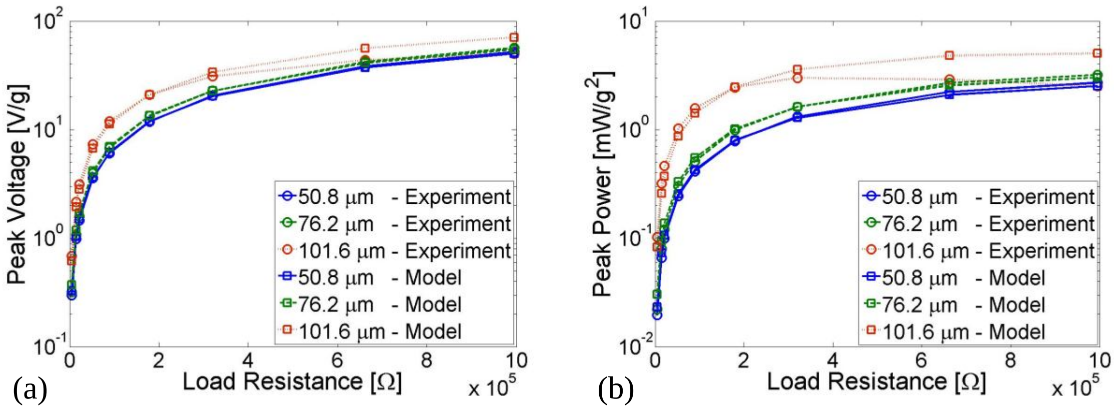

Figure 10. Variations of the (a) peak voltage and (b) peak power outputs of the MFCs with stainless steel substrates with electrical load resistance for excitation at the short circuit resonance frequency of the first mode

4-5. Comparison of different substrates for power generation

Having modeled the 9 MFC unimorph samples shown in Figure 7b, it is aimed in this section to compare performances of all these samples with each other. Therefore, the maximum peak power of each substrate material is plotted against substrate thickness. Figure 11 shows that, for the substrate thicknesses investigated here, 76.2 μm is better for power generation compared to the substrate thicknesses of 50.8 μm and 101.6 μm. Among the substrate materials used, the MFC unimorph with aluminum substrate yields the best power output. A more accurate comparison would be based on the power density (power per overhang volume) or the specific power outputs (power per overhang mass) of these samples. Note that, for a fixed substrate thickness and for similar epoxy thicknesses (compare aluminum and brass in Table 2), the power density trends would not change the superiority of the aluminum substrate. Since the mass density of the aluminum is the lowest among the samples investigated here, comparison of the specific power would again prove the superiority of the unimorph with a 76.2 μm thick aluminum substrate over the others.

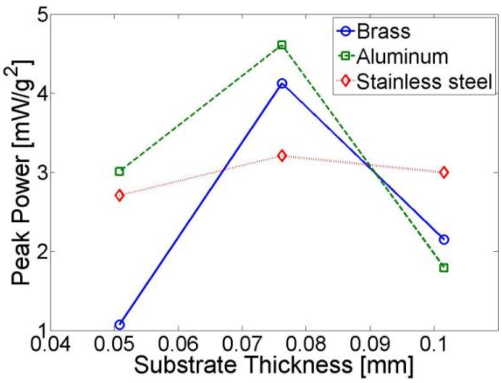

Figure 11. Comparison of the peak power outputs of the MFC unimorphs with different substrate materials and thicknesses for resonance excitation (experimental data)

5. PRELIMINARY RESULTS FOR ENERGY HARVESTING FROM A FLOW-EXCITED MORPHING AIRFOIL

Energy harvesting experiments are conducted on a thin morphing airfoil which has been investigated for MFC actuation by Bilgen *et al* [22]. An illustration of the airfoil in its morphed shape is given in Figure 12. The airfoil (133 mm span and 127 mm chord) is a bimorph with four M 8557 P1 MFC piezoceramic patches (two on the top surface and two on the bottom surface). Only the two patches on the top surface are employed for power generation in this study. The electrical outputs of the two MFC patches are combined in parallel and connected to a resistive electrical load. The substrate material of the airfoil is stainless steel. The morphing airfoil is supported by two revolute joints on each (span-wise) end, which are located at 5 % chord and 50 % chord from the leading edge. The location of chord-wise support points is derived using a structural/aerodynamic optimization procedure presented by Bilgen *et al* [23].

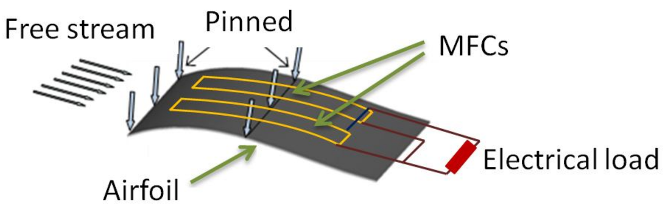

Figure 12. Flow excitation of a morphing airfoil for piezoelectric energy harvesting

The energy harvesting experiments are conducted for 9 different resistive loads (9.76, 21.2, 52.5, 89.5, 106.9, 320, 494, 661.5 and 995 kohms). It should be noted that no actuation voltage is applied to the airfoil; hence the airfoil is simply a flat-plate bimorph. The airfoil is placed in a 137 mm tall (span-wise) and 356 mm wide test section of a wind tunnel. Velocity sweep at 0, 5, 10 and 15 m/s is conducted where an angle of attack (AOA) sweep of 0, 10, 20 and 30 degrees is done for each velocity. The time history of MFC voltage output across the resistive load is measured. Along with the total voltage output of the MFC patches (combined in parallel), the trailing edge velocity of the airfoil is also measured with a laser vibrometer. Velocity and voltage signals are recorded by means of a data acquisition system (SigLab). Times histories of the trailing edge velocity response and voltage response across the resistive load are displayed in Figures 13a and 13b, respectively (for an electrical load resistance of 98 kohms and an AOA of 20 degrees).

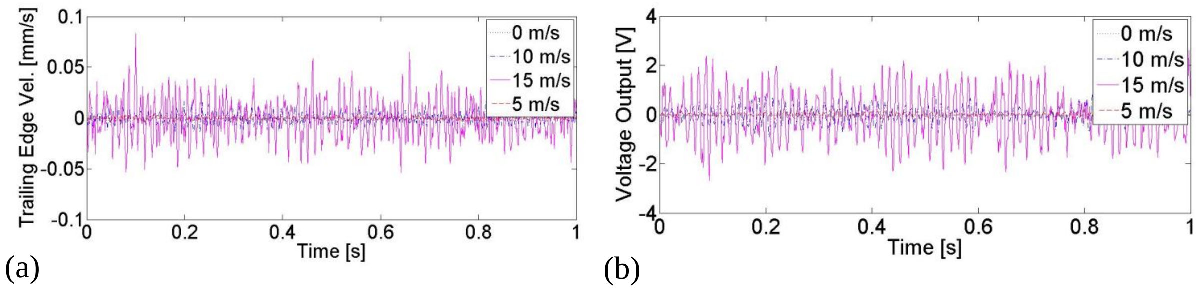

Figure 13. Time histories of the (a) trailing edge velocity response and the (b) voltage output of the MFCs for different flow velocities (for a 98 kohm load resistance and 20 degrees AOA)

Due to the random behavior of the electrical and mechanical response, the RMS (root mean square) values of the electrical power are obtained using 7 seconds of the voltage time history for each value of AOA and flow velocity. Figure 14 shows the RMS power versus load resistance graphs for 4 different values of AOA. In each graph, the RMS power curves are plotted for different flow velocities (including no flow, i.e., zero flow velocity). Expectedly, power output increases with increasing flow velocity. The maximum RMS power is obtained as 7 μW for a 20 deg. AOA and 98 kohm load resistance at a flow velocity of 15 m/s (Figure 14c).

The RMS power values obtained in these preliminary experiments are relatively low compared to typical performance results reported for cantilevered piezoelectric energy harvesters (just like the ones investigated in Sections 3 and 4 of this paper). This is mainly because of the fact that flow excitation is *not* a persistent resonance frequency excitation and its frequency content is not necessarily close to a resonance frequency of the airfoil. As can be seen from the trailing edge velocity and voltage response histories given for the optimum load resistance and AOA (Figure 13), the time histories of the electrical and mechanical responses are fairly random. One would expect much larger power outputs if the airfoil was excited around one of its resonance frequencies (preferably at the fundamental resonance frequency). It should be noted that larger power outputs means stronger vibrations of the airfoil. Therefore, in practice, the trade-off is between the stable behavior of the aircraft wing and the amplitude of the electrical power output.

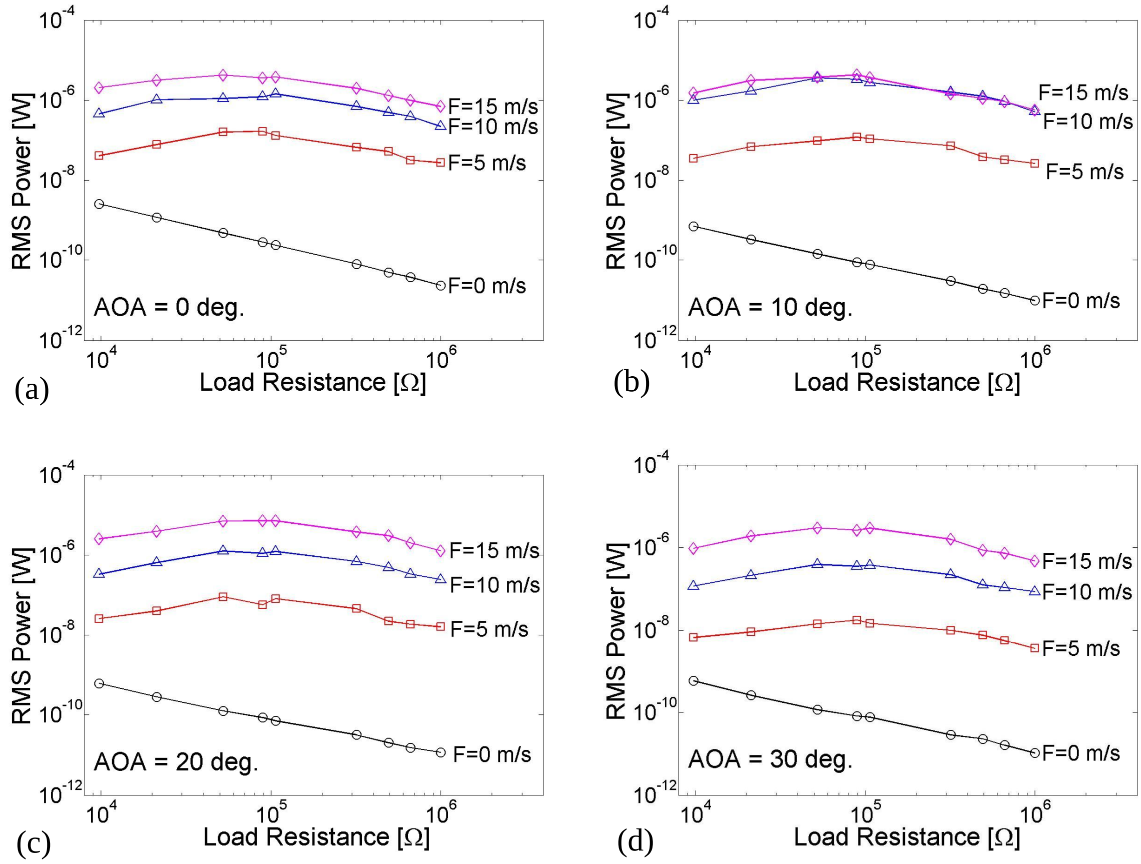

Figure 14. Variation of the electrical RMS power with load resistance for different values of AOA; (a) AOA=0 deg., (b) AOA=10 deg., (c) AOA=20 deg., (d) AOA=30 deg.

6. CONCLUSIONS

Piezoelectric energy harvesting has been investigated by several researchers for vibration-based energy harvesting in the last five years. Typically, a piezoelectric energy harvester is a unimorph or a bimorph with monolithic piezoceramic layers. There are several excitation types and operation environments where conventional monolithic piezoceramics cannot be used due to their brittle nature. The MFC configuration constitutes a unique alternative to monolithic piezoceramics due to its robust and flexible nature.

In this work, a distributed-parameter electromechanical model is proposed for predicting the coupled mechanical and electrical response of MFC unimorphs for piezoelectric energy harvesting. The model proposed here is based on a recently proposed closed-form solution for a monolithic unimorph. Modeling steps are given in detail and correction factors are introduced in order to handle the non-uniform electric field of the MFC configuration. After obtaining the relations for the voltage response and the vibration response at steady state, model verification is presented for an MFC unimorph with a brass substrate. It is shown that the model presented here can successfully predict the coupled dynamics of the MFC unimorph for a wide range of electrical load resistance.

Then, a set of MFC unimorphs with different substrate materials and thicknesses are tested and modeled. Among the samples studied, the best substrate material and thickness ratio are identified for the maximum power generation. The results of this analysis are predicted by the coupled model successfully. Finally, results from the preliminary wind tunnel experiments are presented for piezoelectric energy harvesting from a flow-excited morphing airfoil with MFCs as an introduction to energy harvesting from MFCs of morphing-wing aircrafts.

ACKNOWLEDGEMENTS

The authors gratefully acknowledge the support of the Air Force Office of Scientific Research MURI under grant number F 9550-06-1-0326 "Energy Harvesting and Storage Systems for Future Air Force Vehicles" monitored by Dr. B. L. Lee. Mr. A. Erturk acknowledges the support from the Liviu Librescu Memorial Scholarship of the Department of Engineering Science and Mechanics at Virginia Tech.

REFERENCES

1. Glynne-Jones P, Tudor M J, Beeby S P and White N M 2004 An electromagnetic, vibration-powered generator for intelligent sensor systems *Sensors and Actuators A* 110:344-349
2. Arnold D 2007 Review of microscale magnetic power generation *IEEE Transactions on Magnetics* 43:3940–3951
3. Roundy S, Wright P K and Rabaey J 2002 Micro-electrostatic vibration-to-electricity converters *Proceedings of the ASME 2002 International Mechanical Engineering Congress and Exposition*
4. Mitcheson P, Miao P, Start B, Yeatman E, Holmes A and Green T 2004 MEMS electrostatic micro-power generator for low frequency operation *Sensors and Actuators A* 115:523-529
5. Roundy S, Wright P K and Rabaey J 2003 A study of low level vibrations as a power source for wireless sensor nodes *Computer Communications* 26:1131-1144
6. Jeon Y B, Sood R, Jeong J H and Kim S 2005 MEMS power generator with transverse mode thin film PZT *Sensors & Actuators A* 122:16-22
7. Sodano H A, Inman D J and Park G 2004 A review of power harvesting from vibration using piezoelectric materials *The Shock and Vibration Digest* 36:197-205
8. Priya S 2007 Advances in energy harvesting using low profile piezoelectric transducers *Journal of Electroceramics* 19:167–184
9. Anton S R and Sodano H A 2007 A review of power harvesting using piezoelectric materials (2003-2006) *Smart Materials and Structures* 16:R1-R21
10. Cook-Chennault K A, Thambi N, Sastry A M 2008 Powering MEMS portable devices – a review of non-regenerative and regenerative power supply systems with emphasis on piezoelectric energy harvesting systems *Smart Materials and Structures* 17:043001:1-33
11. Wilkie W K, Bryant G R and High J W, Low-cost piezocomposite actuator for structural control applications *SPIE 7th Annual International Symposium on Smart Structures and Materials*, Newport Beach, CA, 2000
12. Park G, Ruggiero E and Inman D J 2002 Dynamic testing of an inflattable structure using smart materials *Smart Materials and Structures*, 11:147–166
13. Adachi K, Park G and Inman D J 2002 Passive damping augmentation using macro-fiber composite actuators *Proc. ASME Int. Mech. Engrg Congr. Expo*, pages 71–78, New Orleans, USA, 2002.
14. Deraemaeker A, Benelechi S, Benjeddou A and Preumont, A 2007 Analytical and numerical computation of homogenized properties of MFCs: Application to a composite boom with MFC actuators and sensors, *Proceedings of III ECOOMAS Thematic Conference on Smart Structures and Materials*, Gdansk, Poland, 9-11 July 2007
15. Sodano H A, Lloyd Sodano H A, Lloyd J and Inman D J 2006 An experimental comparison between several active composite actuators for power generation *Smart Mater. Struct.* 15 1211–6
16. Lloyd, J 2004 *Electrical properties of macro-fiber composite actuators and sensors*, MS thesis, Virginia Polytechnic Institute and State University, Blacksburg, VA
17. Berger H *et al* 2006 Unit cell models of piezoelectric fiber composites for numerical and analytical calculation of effective properties. *Smart Mater. Struct.*, 15:451–458, 2006
18. Erturk A and Inman D J 2008 A distributed parameter electromechanical model for cantilevered

piezoelectric energy harvesters *ASME Journal of Vibration and Acoustics* 130:041002
19. Erturk A and Inman D J 2009 An experimentally validated bimorph cantilever model for piezoelectric energy harvesting from base excitations *Smart Materials and Structures* accepted
20. *IEEE Standard on Piezoelectricity* 1988 IEEE, New York.
21. Smart Material (http://www.smart-material.com)
22. Bilgen O, Erturk A and Inman D J Macro-Fiber Composite Actuated Thin Clamped-Free Benders and Thin Simply-Supported Morphing Airfoils, *19th International Conference on Adaptive Structures and Technologies*, October 6-9, 2008, Ascona, Switzerland (on CD)
23. Bilgen O, Kochersberger K B and Inman D J 2008 A novel aerodynamic vectoring control airfoil via macro-fiber-composite actuators *49th AIAA/ASME/ASCE/AHS/ASC Structures, Structural Dynamics, and Materials Conference*, Schaumburg, IL, 7 - 10 April 2008, AIAA 2008-1700